

**Visible light excited Yb³⁺-doped phosphor via Eu²⁺ bridged
energy transfer towards NIR-II spectroscopy application**

Zhuowei Li,^{a,b} Ge Zhu,^{b,*} Heyang Li,^c Qi Zhu,^a Yan Cong,^b Xue Bai,^d Ji-Guang Li,^{e,*}

Bin Dong^{b*}

^a *Key Laboratory for Anisotropy and Texture of Materials (Ministry of Education),
School of Materials Science and Engineering, Northeastern University, Shenyang,
Liaoning 110819, P. R. China*

^b *Key Laboratory of New Energy and Rare Earth Resource Utilization of State Ethnic
Affairs Commission, Key Laboratory of Photosensitive Materials & Devices of
Liaoning Province, College of Physics and Materials Engineering, Dalian Minzu
University, Dalian, Liaoning 116600, P. R. China*

^c *Department of Physics & Astronomy, University College London, United Kingdom*

^d *Key Laboratory of Integrated Optoelectronics and College of Electronic Science and
Engineering, Jilin University, Changchun, Jilin 130012, P. R. China*

^e *Research Center for Electronic and Optical Materials, National Institute for Materials
Science, Tsukuba, Ibaraki 305-0044, Japan*

*Corresponding author

Prof. Bin Dong

Dalian Minzu University

E-mail: dong@dlnu.edu.cn

Dr. Ji-Guang Li

National Institute for Materials Science

E-mail: li.jiguang@nims.go.jp

Prof. Ge Zhu

Dalian Minzu University

E-mail: zhuge@dlnu.edu.cn

Abstract

Yb^{3+} is regarded as an efficient near-infrared-II (NIR-II) emitting activator, which has been widely used in energy conversion, up-conversion luminescence and optical communication. However, the simple energy level structure of Yb^{3+} makes it can only be excited by ultraviolet or infrared light, which limits their application in the currently booming phosphor converted near-infrared-II light emitting diodes (NIR-II pc-LEDs). Here, we presented “ Eu^{2+} bridge” strategy to extend Yb^{3+} absorption to visible range, and successfully realize efficient visible light pumped NIR-II emission via energy transfer from Eu^{2+} to Yb^{3+} . Meanwhile, to balance the valence state of reduced Eu^{2+} and oxidized Yb^{3+} , the pre-prepared EuS was used as precursor instead of Eu_2O_3 , which significantly increases the NIR-II luminescence of Yb^{3+} by 6 times. Detailed energy transfer and luminescence enhancement mechanism were discussed. Finally, a NIR-II pc-LED was fabricated with photoelectric efficiency of 12.61%@50 mA and output power of 74.09 mW@300 mA. Subsequently, a miniaturized and real-time test system was integrated based on the convolutional neural network technology to accurate predict organic solvents with different concentrations. This study not only introduces a new strategy to realize visible light excited Yb^{3+} -doped NIR-II emitting phosphors, but also promotes their innovative application based on NIR spectroscopy technology.

Keywords: garnet structure; Yb^{3+} ions; energy transfer; NIR-II pc-LEDs; convolutional neural network technology.

1 **1. Introduction**

2 In recent years, the portable near-infrared-II (NIR-II) light sources, which can be
3 easily integrated into smartphones and wearable devices, have exhibited broad
4 application prospects in various fields such as non-destructive testing, medical
5 diagnosis, and food quality assessment.¹⁻³ Phosphor converted near-infrared-II light
6 emitting diodes (NIR-II pc-LEDs), considered ideal for next generation portable NIR-
7 II light sources, are expected to replace traditional tungsten halogen lamps and lasers
8 due to their noteworthy attributes of high efficiency, compact design and good
9 durability.^{4, 5} Currently, one of the most widely used NIR pc-LED is the SFH 4735
10 introduced by OSRAM in 2016.^{6, 7} Unfortunately, the emission intensity of this NIR pc-
11 LED in the NIR-II region (900–1050 nm) is significantly lower than that in the NIR-I
12 region (650–900 nm), limiting its use in food detection (~970 nm) and long-wavelength
13 fluorescent probes (~1000 nm).⁸ Although OSRAM has subsequently developed the
14 SFH 4737 NIR pc-LED light source,⁹ and researchers have also developed a variety of
15 NIR pc-LED devices based on fluorine and oxide luminescent materials.¹⁰⁻¹⁶ There is
16 still a lack of effective means to broaden the spectral range of the NIR-II region and
17 improve the luminous intensity, which is a huge challenge.

18 As a key component of NIR-II pc-LED, the luminescence characteristics of NIR-
19 II emitting phosphors directly affect the spectral range, conversion efficiency and
20 output power of the device. Currently, Eu^{2+} and Cr^{3+} ions are among the most widely
21 used activators for generating NIR emission.¹⁷⁻²⁰ However, despite substantial efforts,
22 the NIR emission wavelength of Eu^{2+} ions still remains difficult to significantly extend

1 to longer wavelengths ($\lambda_{\text{em}} > 900 \text{ nm}$).¹¹ Cr^{3+} ion in a strong crystal field environment
2 will show the narrow-band emission characteristics related to the ${}^2\text{E}_g \rightarrow {}^4\text{A}_{2g}$ transition.
3 On the contrary, it will exhibit broadband emission caused by the spin-allowed ${}^4\text{T}_{2g} \rightarrow$
4 ${}^4\text{A}_{2g}$ transition. Therefore, Cr^{3+} -activated phosphors usually exhibit long-wavelength
5 emission and excellent NIR luminescence properties.^{21,22} Unfortunately, they are prone
6 to oxidation during high-temperature processing, transforming into harmful Cr^{4+} and
7 Cr^{6+} forms.²³ The rare-earth ion Yb^{3+} is widely regarded as a highly efficient activator
8 for NIR-II emission with a peak wavelength approximately at 1000 nm.²⁴ However, the
9 parity-forbidden 4f-4f transition characteristic of Yb^{3+} ions results in its weak light
10 absorption capacity. Additionally, the $4f^{13}$ electronic configuration restricts Yb^{3+} ions to
11 only two energy levels: the ${}^2\text{F}_{7/2}$ ground state and the ${}^2\text{F}_{5/2}$ excited states. Consequently,
12 Yb^{3+} ions can only be excited by ultraviolet (e.g. Yb^{3+} -ligand charge transfer band) or
13 infrared light (${}^2\text{F}_{7/2} \rightarrow {}^2\text{F}_{5/2}$ transition),²⁵⁻²⁷ but cannot be excited by the commonly used
14 visible LED chips. Thus, developing Yb^{3+} -doped NIR-II emitting phosphors for
15 portable pc-LED applications remains a significant challenge.

16 Constructing an efficient energy transfer “bridge” to sensitize Yb^{3+} ions emission
17 is considered as an effective strategy to address this problem. At present, Cr^{3+} ions are
18 the main activator ion to sensitize Yb^{3+} ions.²⁸⁻³⁰ However, due to the parity-forbidden
19 transition inherent to Cr^{3+} ions, their excitation spectra typically exhibit strong
20 absorption in the blue light region, making it challenging to achieve efficient emission
21 excited by other visible light. In contrast, Eu^{2+} usually possesses efficient broadband

1 excitation due to its parity-allowed $4f^65d^1 \rightarrow 4f^7$ transitions.³¹⁻³³ Moreover, the excitation
2 and emission energy of Eu^{2+} can be easily adjusted in the whole visible light region
3 depending on different crystal field strength,³⁴⁻³⁷ which is more suitable to realize the
4 visible light excitation of Yb^{3+} through energy transfer.

5 Garnet-type compounds are considered as ideal host materials for luminescent
6 materials because of their deliberate luminescent properties and abundant cation sites,
7 which have important applications in white LED, optical anti-counterfeiting, biological
8 imaging, solar cells and so on.³⁸⁻⁴⁰ Among them, Zhou et al. reported a garnet-based
9 solar cell light-converting material based on the energy transfer from Ce^{3+} to Eu^{2+} and
10 finally to Yb^{3+} ions, utilizing the carbothermal reduction method.⁴¹ However, the
11 quantum efficiency of Eu^{2+} , Yb^{3+} co-doped sample is only 7.9%, insufficient for current
12 NIR spectroscopy applications. The reason may be that Eu^{3+} ions cannot be completely
13 reduced to Eu^{2+} in a weak reducing atmosphere, and some Yb^{3+} ions may be reduced to
14 Yb^{2+} ions, which ultimately hinders the energy transfer process. Thus, there is an urgent
15 need to develop effective strategies to balance the valence states of reduced Eu^{2+} ions
16 and oxidized Yb^{3+} ions, thereby enhancing the NIR-II luminescence of Yb^{3+} ions via
17 Eu^{2+} ions sensitization.

18 In this work, a series of NIR-II emitting garnet phosphors $\text{Ca}_3\text{Sc}_2\text{Si}_3\text{O}_{12}: x\text{Eu}^{2+}$,
19 $y\text{Yb}^{3+}$ (CSSO: $x\text{Eu}^{2+}$, $y\text{Yb}^{3+}$, $x = 0$ and 1%, $0 \leq y \leq 7\%$) are synthesized using the pre-
20 prepared EuS instead of traditional Eu_2O_3 as dopant under N_2 atmosphere. The result
21 indicates that the proposed strategy not only realizes the NIR-II emission of Yb^{3+} ions

by visible light excitation, but also effectively inhibits the formation of Eu^{3+} and Yb^{2+} ions and enhances the energy transfer from Eu^{2+} to Yb^{3+} ions, resulting in the largely increased NIR-II luminescence by 6 times. Furthermore, we successfully fabricated a portable NIR-II pc-LED based on the optimized CSSO: 1% Eu^{2+} , 5% Yb^{3+} , and used absorption spectroscopy techniques in conjunction with convolutional neural network (CNN) technology to achieve accurate prediction of various organic solvents at different concentrations. We hope that this study will inspire the development of Yb^{3+} activated NIR-II emitting phosphors and their innovative application based on NIR spectroscopy technology in the future.

2. Results and discussion

2.1 Phase purity and structure transition analysis of CSSO: Eu^{2+} , Yb^{3+} samples.

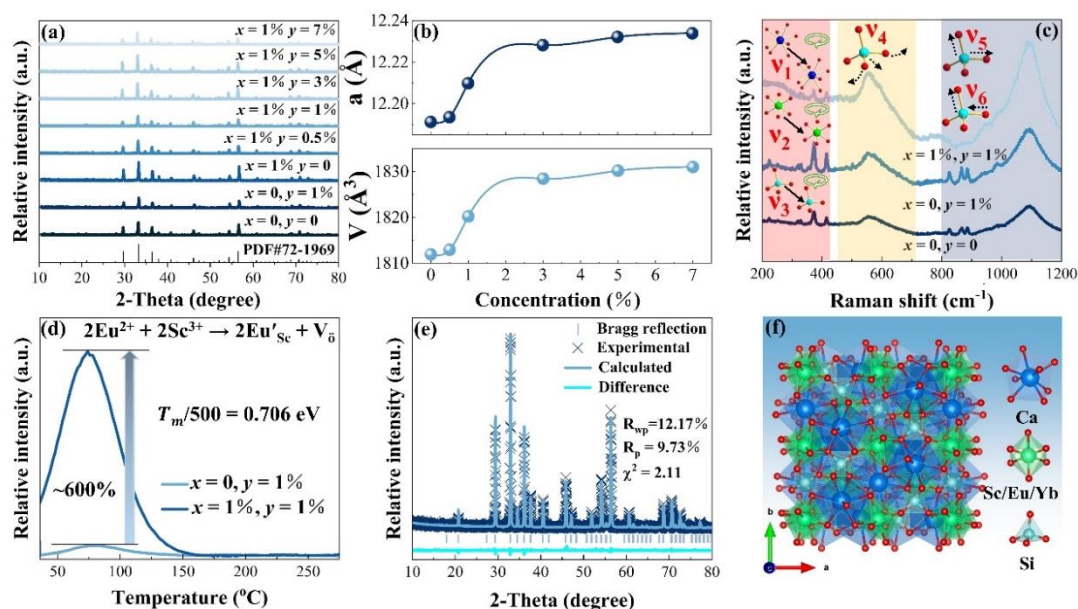


Figure 1(a) The XRD patterns of CSSO: $x\text{Eu}^{2+}$, $y\text{Yb}^{3+}$ ($x=0$ and 1%, $0 \leq y \leq 7\%$) samples; (b) The crystallographic parameters a and V of CSSO: 1% Eu^{2+} , $y\text{Yb}^{3+}$ ($0 \leq y \leq 7\%$) samples; (c) The Raman spectra of CSSO, CSSO: 1% Yb^{3+} and CSSO: 1% Eu^{2+} , 1% Yb^{3+} samples; (d) The thermoluminescence curve of CSSO: 1% Yb^{3+} and CSSO: 1% Eu^{2+} , 1% Yb^{3+} samples excited for 10 min; (e) Rietveld refinement of the XRD pattern for CSSO: 1% Eu^{2+} , 5% Yb^{3+} sample; (f) The crystal structure of CSSO: 1% Eu^{2+} , 5% Yb^{3+} sample.

1 Figure 1a presents the XRD patterns of CSSO: $x\text{Eu}^{2+}$, $y\text{Yb}^{3+}$ ($x = 0$ and 1% , $0 \leq y$
 2 $\leq 7\%$) samples. The diffraction peaks observed in all synthesized samples are
 3 completely consistent with the standard data for $\text{Ca}_3\text{Sc}_2\text{Si}_3\text{O}_{12}$ (PDF#72-1969),
 4 confirming the successful synthesis of pure-phase phosphors. Notably, the
 5 crystallographic parameters a and V of CSSO: $1\%\text{Eu}^{2+}$, $y\text{Yb}^{3+}$ ($0 \leq y \leq 7\%$) samples
 6 follow Vegard's law.⁴² That is, the crystallographic parameters gradually increase due
 7 to the larger ionic radii of Yb^{3+} ions (CN = 6, $R = 0.868 \text{ \AA}$) compared with those of Sc^{3+}
 8 ions (CN = 6, $R = 0.745 \text{ \AA}$) (Fig. 1b),⁴³ which is also confirmed by the low-angle shift
 9 of the XRD pattern peak as shown in Fig. S1. According to the previous analysis,
 10 broadband NIR emission will generate when Eu^{2+} ions occupy the six-coordinated Sc^{3+}
 11 sites.⁴⁴ To further explore the effect of doping Yb^{3+} and Eu^{2+} ions on the crystal structure
 12 of the samples, the Raman spectra of CSSO, CSSO: $1\%\text{Yb}^{3+}$ and CSSO: $1\%\text{Eu}^{2+}$,
 13 $1\%\text{Yb}^{3+}$ samples are measured. As shown in the Fig. 1c, the vibrational modes in the
 14 range of $200\text{--}415 \text{ cm}^{-1}$ originate from the rotational and translational motions of the
 15 CaO_8 dodecahedra (v_1), ScO_6 octahedra (v_2) and SiO_4 tetrahedra (v_3). The vibrational
 16 modes lying from 450 to 700 cm^{-1} are assigned to bending motions of SiO_4 tetrahedra
 17 (v_4). The vibration modes within the range of $800\text{--}1200 \text{ cm}^{-1}$ are attributed to the
 18 symmetric (v_5) and asymmetric (v_6) internal stretching vibrations of the SiO_4
 19 tetrahedra.⁴⁵⁻⁴⁷ It is worth noting that the Raman peak of CSSO: Yb^{3+} sample does not
 20 shows significantly shift or broadening compared with CSSO sample. However, when
 21 Eu^{2+} and Yb^{3+} ions are co-doped, the Raman peak broadening is observed in the range

1 of 200–300 cm^{-1} and 800–900 cm^{-1} . This broadening may arise from the unbalanced
 2 substitution of Eu^{2+} for Sc^{3+} ions, which destroys the lattice order in the crystal
 3 structure.⁴⁸ To further verify the above inference, we perform the electron paramagnetic
 4 resonance (EPR) test on CSSO: 1% Eu^{2+} , 1% Yb^{3+} sample, as shown in Fig. S2. The
 5 EPR signals at $g = 6.1$, 4.4 and 2.7 are corresponding to the unpaired electrons in Eu^{2+}
 6 ions.^{49,50} The EPR signal at $g = 2$ originates from electrons trapped in oxygen vacancies.
 7 ⁵¹ However, no EPR signal is detected in the CSSO: 1% Yb^{3+} sample. The
 8 thermoluminescence spectra of CSSO: 1% Yb^{3+} and CSSO: 1% Eu^{2+} , 1% Yb^{3+} samples
 9 also provide strong evidence for the above inference, as shown in Fig. 1d. The intensity
 10 of the main thermoluminescence peak (80°C) of the CSSO: 1% Eu^{2+} , 1% Yb^{3+} sample is
 11 600% higher than that of CSSO: 1% Yb^{3+} sample, and the trap depth is calculated to be
 12 0.706 eV. This phenomenon indicates that the unbalanced substitution of Eu^{2+} for Sc^{3+}
 13 significantly increases the oxygen vacancies concentration,⁵² as represented by the
 14 reaction: $2\text{Eu}^{2+} + 2\text{Sc}^{3+} \rightarrow 2\text{Eu}'_{\text{Sc}} + \text{V}_{\text{O}}$. This further supports the above view that Eu^{2+}
 15 ions can replace Sc^{3+} ions, thereby reducing the order of CSSO host. In addition, to
 16 obtain structural information of the CSSO: 1% Eu^{2+} , 5% Yb^{3+} sample, the Rietveld
 17 refinement of XRD pattern is performed using garnet $\text{Ca}_3\text{Sc}_2\text{Si}_3\text{O}_{12}$ as the initial model,
 18 as shown in Fig. 1e. The refined parameters $R_{\text{wp}} = 12.17\%$, $R_{\text{p}} = 9.73\%$ and $\chi^2 = 2.11$,
 19 indicating the reliability of the refined structural model.⁵³ The refined cell parameters,
 20 atomic sites and bond lengths are listed in the Table S1-S3, respectively. CSSO: 1% Eu^{2+} ,
 21 5% Yb^{3+} sample exhibits a cubic crystal structure in the Ia-3d(230) space group, with a

cell parameter $a = 12.23 \text{ \AA}$ and cell volume $V = 1829.28 \text{ \AA}^3$. Based on the refinement results, the crystal structure of the CSSO: 1% Eu^{2+} , 5% Yb^{3+} sample is illustrated in Fig. 1f. This structure consists primarily of CaO_8 dodecahedra, $\text{Sc}/\text{Eu}/\text{YbO}_6$ octahedra and SiO_4 tetrahedra, with average bond lengths of 2.48, 2.09 and 1.64 \AA (Table S3), respectively. Additionally, the $\text{Sc}/\text{Eu}/\text{YbO}_6$ octahedra share edges with CaO_8 dodecahedra, and vertices with the SiO_4 tetrahedra, thus forming a stable unit mode.

2.2 Morphological, XPS and EDS analysis of CSSO: Eu^{2+} , Yb^{3+} sample.

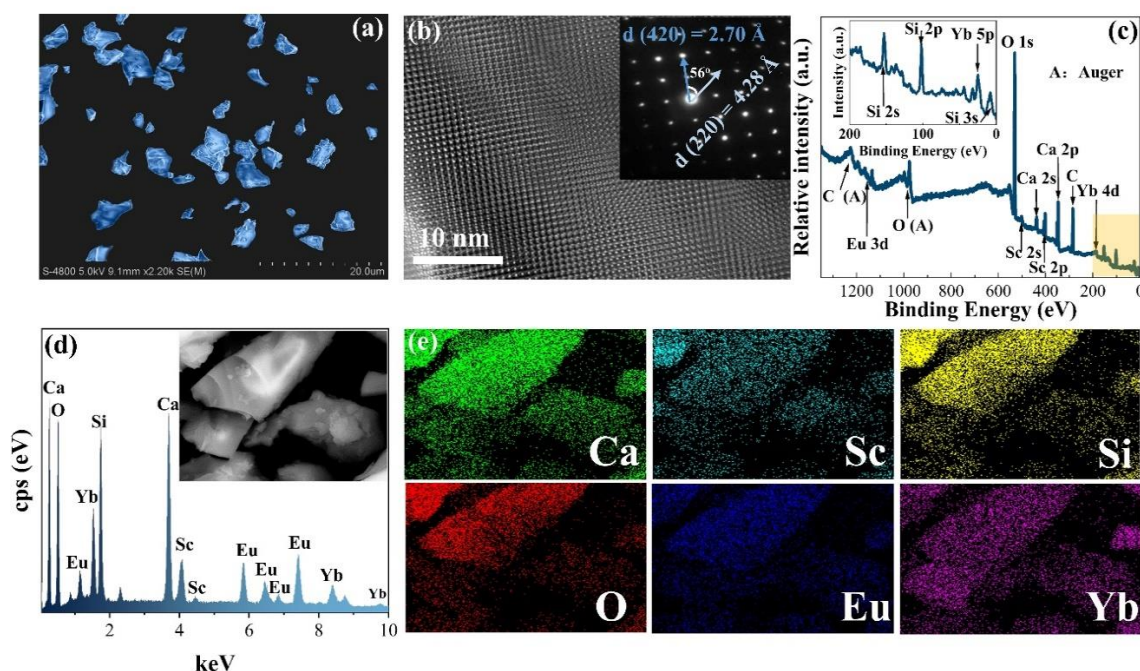


Figure 2(a) and (b) The SEM, HR-TEM and SAED images of CSSO: 1% Eu^{2+} , 5% Yb^{3+} sample; (c) The XPS spectrum of CSSO: 1% Eu^{2+} , 5% Yb^{3+} sample, the inset shows an enlarged view of the yellow region; (d) and (e) The EDS spectrum and elemental mapping of CSSO: 1% Eu^{2+} , 5% Yb^{3+} sample particles.

The scanning electron microscope (SEM) images and particle size distribution histograms of CSSO: 1% Eu^{2+} , 5% Yb^{3+} sample are given in Fig. 2a and S3, with an average particle size of 3.3 μm . In addition, a single particle has undergone high-resolution transmission electron microscopy (HR-TEM) and selected area electron diffraction (SAED) analysis, as illustrated in Fig. 2b. The HR-TEM image indicates

1 that the sample possesses good crystallinity, and the lattice stripe spacings of 2.70 and
2 4.28 Å, calculated from the SAED pattern clearly reveal the existence of (420) and (220)
3 planes of the garnet structure $\text{Ca}_3\text{Sc}_2\text{Si}_3\text{O}_{12}$. In order to study the electronic states and
4 charges of the elements in CSSO: 1% Eu^{2+} , 5% Yb^{3+} sample, we have used X-ray
5 photoelectron spectroscopy (XPS) technology to analyze them. The XPS spectrum and
6 the core level spectra of all elements are shown in Fig. 2c and S4, respectively. The
7 characteristic peaks at 347, 402, 102, 532, 1154 and 185 eV are observed, corresponding
8 to the energy level characteristics of Ca 2p, Sc 2p, Si 2p, O 1s, Eu 3d and Yb 4d,
9 respectively. These results further confirm the successful preparation of CSSO: 1% Eu^{2+} ,
10 5% Yb^{3+} sample. Furthermore, the elemental composition and distribution of CSSO:
11 1% Eu^{2+} , 5% Yb^{3+} sample are analyzed using the energy dispersive spectroscopy (EDS),
12 as shown in Fig. 2d and 2e. The EDS spectrum and elemental mapping further confirm
13 that Eu^{2+} and Yb^{3+} ions are successfully doped into the host as well as the uniform
14 distribution of Ca, Sc, Si, O, Eu and Yb in the phosphor particles.

2.3 The luminescence properties and energy transfer analysis of the CSSO: Eu^{2+} , Yb^{3+} samples.

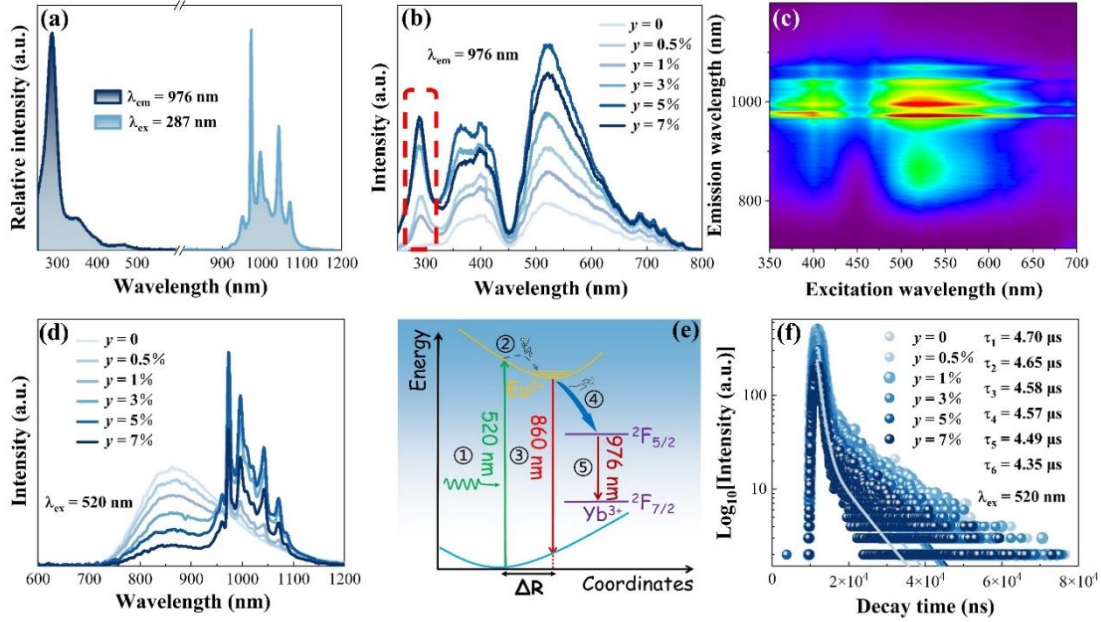


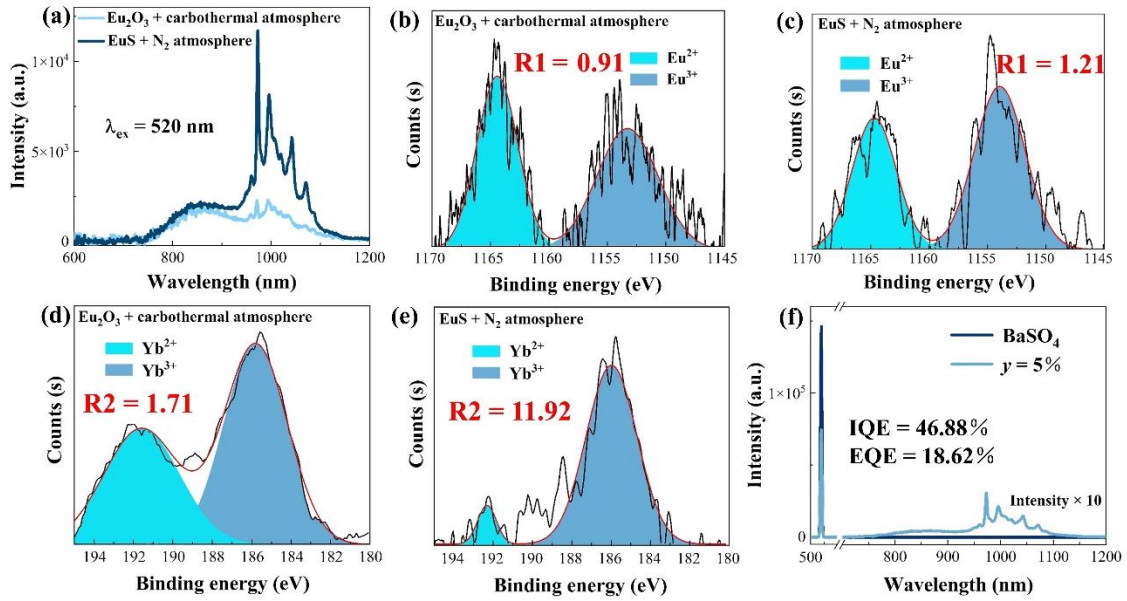
Figure 3(a) The excitation and emission spectra of CSSO: 1% Yb^{3+} sample; (b) The excitation spectra of CSSO: 1% Eu^{2+} , $y\text{Yb}^{3+}$ ($0 \leq y \leq 7\%$) samples; (c) The emission spectra mapping at different excitation wavelengths ($\lambda_{\text{ex}} = 350-700$ nm); (d) The emission spectra of CSSO: 1% Eu^{2+} , $y\text{Yb}^{3+}$ ($0 \leq y \leq 7\%$) samples; (e) The schematic diagram of the energy transfer process from Eu^{2+} to Yb^{3+} ions in the CSSO: Eu^{2+} , Yb^{3+} sample; (f) The decay curves of CSSO: 1% Eu^{2+} , $y\text{Yb}^{3+}$ ($0 \leq y \leq 7\%$) samples.

Figure 3a shows the excitation and emission spectra of CSSO: 1% Yb^{3+} sample. Specifically, the NIR-II emission centered at 976 nm can be clearly observed under the UV light excitation, attributed to the $^2\text{F}_{5/2} \rightarrow ^2\text{F}_{7/2}$ transition of Yb^{3+} ions. Simultaneously, a broad excitation band ranging from 270 to 400 nm is recorded when monitoring the emission at 976 nm, attributed to the $\text{Yb}^{3+}-\text{O}^{2-}$ charge transfer bands.²⁵ As we know, the presence of Eu^{3+} and Yb^{2+} ions will significantly hinder the NIR luminescence of Eu^{2+} and Yb^{3+} ions in CSSO host. To address this issue, we utilized pre-prepared EuS as a raw material to substitute for the commonly used Eu_2O_3 and synthesized a series of garnet structure CSSO: 1% Eu^{2+} , $y\text{Yb}^{3+}$ ($0 \leq y \leq 7\%$) samples under N_2 atmosphere, the

1 excitation spectra of these samples are presented in the Fig. 3b. At a monitored of 976
 2 nm, the excitation spectra of the Eu^{2+} and Yb^{3+} co-doped samples, compared to the
 3 spectrum of the Yb^{3+} -doped sample, not only exhibit the characteristic excitation of
 4 Yb^{3+} - O^{2-} charge transfer bands, but also reveals strong absorption in visible light region,
 5 corresponding to the $4f \rightarrow 5d$ transitions of Eu^{2+} ions, which indicates that there exists
 6 effective energy transfer between Eu^{2+} and Yb^{3+} ions. In addition, CSSO: Eu^{2+} , Yb^{3+}
 7 samples can be effectively excited by almost the entire visible light (350–700 nm) and
 8 emit broad NIR-II emission, as shown in Fig. 3c and S5. Under the optimal excitation
 9 of 520 nm, the emission spectra simultaneously display the broadband NIR-I emission
 10 of Eu^{2+} ions at 860 nm, along with the characteristic NIR-II emission peak of Yb^{3+} ions
 11 at 976 nm, attributed to $5d \rightarrow 4f$ and ${}^2\text{F}_{5/2} \rightarrow {}^2\text{F}_{7/2}$ transition, respectively. It is noteworthy
 12 that the emission intensity of Eu^{2+} ions significantly decreases with the increase of Yb^{3+}
 13 concentration, which confirms the existence of energy transfer between Eu^{2+} and Yb^{3+}
 14 ions.⁵⁴ Meanwhile, the NIR-II emission intensity of Yb^{3+} ions reaches its maximum at
 15 a concentration of 5%, as shown in Fig. 3d. To better understand the energy transfer
 16 process from Eu^{2+} to Yb^{3+} ions, a schematic of the energy transfer is constructed, as
 17 shown in Fig. 3e. Upon 520 nm excitation, the electrons are excited to the 5d excited
 18 state of Eu^{2+} ions, and then transfer to the ${}^2\text{F}_{5/2}$ excited state of Yb^{3+} based on the electric
 19 multipole resonant energy transfer, and finally resulting in the NIR-II luminescence
 20 enhancement of Yb^{3+} ions through ${}^2\text{F}_{5/2}$ to ${}^2\text{F}_{7/2}$ transitions. Moreover, the decay time of
 21 CSSO: 1% Eu^{2+} , $y\text{Yb}^{3+}$ ($0 \leq y \leq 7\%$) samples monitored at 860 nm decrease from 4.70

1 to 4.35 μs (Fig. 3f), further strongly supporting the energy transfer process from Eu^{2+}
2 to Yb^{3+} ions.⁵⁵ As Yb^{3+} ions doping concentration increases, the energy transfer
3 efficiency is evaluated, gradually rising to a maximum of 78.44% at $y = 7\%$, as shown
4 in Fig. S6. This increase of the energy transfer efficiency can be attributed to the
5 shortened distance between sensitizer and activator, effectively enhancing the energy
6 transfer from Eu^{2+} to Yb^{3+} ions.⁵⁶

7 **2.4 Stabilization of Eu^{2+} and Yb^{3+} valence state and luminescence enhancement**
8 **mechanism investigation.**



9
10 Figure 4(a) The emission spectra of CSSO: 1% Eu^{2+} , 5% Yb^{3+} sample with Eu_2O_3 as raw
11 material in a carbothermal atmosphere and EuS as raw material in a N_2 atmosphere; (b) and (d)
12 The XPS spectra of Eu 3d and Yb 4d energy levels of CSSO: 1% Eu^{2+} , 5% Yb^{3+} sample with Eu_2O_3
13 as raw material in a carbothermal atmosphere; (c) and (e) The XPS spectra of Eu 3d and Yb 4d
14 energy levels with EuS as raw material in a N_2 atmosphere; (f) The QE of CSSO: 1% Eu^{2+} ,
15 5% Yb^{3+} sample prepared by EuS in N_2 atmosphere.

16 To substantiate that samples prepared using EuS under N_2 atmosphere enhance the
17 NIR-II emission performance of Yb^{3+} ions, we compared the emission intensity of
18 samples prepared by Eu_2O_3 in a carbothermal atmosphere with those synthesized using

1 the aforementioned method. The NIR-II emission intensity of the sample prepared by
2 our proposed method is 6 times higher than that of the sample prepared by Eu_2O_3 in a
3 carbothermal atmosphere, as shown in Fig. 4a. To gain a deeper understanding of the
4 luminescence enhancement mechanism, the valence state of Eu and Yb is analyzed in
5 detail by XPS spectra. As shown in Fig. 4b and 4c, the Eu 3d XPS spectrum has been
6 deconvoluted into two signal peaks through Gaussian fitting, attributed to Eu^{2+} and Eu^{3+}
7 ions, respectively.⁵⁷ In order to more clearly quantify the XPS signal intensity
8 relationship between Eu^{2+} and Eu^{3+} ions, the XPS signal intensity ratio R1 has been
9 proposed, specifically defined as the ratio of XPS signal intensity between Eu^{2+} and
10 Eu^{3+} ions. Excitingly, the R1 value of EuS-doped sample is 1.21, significantly higher
11 than that of Eu_2O_3 -doped sample ($R1 = 0.91$), indicating a higher content of Eu^{2+} ions
12 in the EuS-doped sample. Additionally, Gaussian fitting is applied to deconvolute the
13 XPS spectra of the Yb^{3+} 4d peak within the range of 180 to 200 eV. The results indicate
14 that the peak at lower energy (~ 192 eV) corresponds to Yb^{2+} ions, while the peak at
15 higher energy (~ 186 eV) corresponds to Yb^{3+} ions.⁵⁸⁻⁶⁰ The XPS signal intensity ratio
16 R2 of Yb^{3+} and Yb^{2+} ions in the powder synthesized in N_2 atmosphere ($R2 = 11.92$) is
17 much higher than that in the carbothermal atmosphere ($R2 = 1.71$) as shown in Fig. 4d
18 and 4e. In addition, the internal and external quantum efficiency (IQE and EQE) of
19 CSSO: 1% Eu^{2+} , 5% Yb^{3+} sample prepared with EuS as the raw material under N_2
20 atmosphere reach 44.68% and 18.62%, respectively, which is 6 times higher than that
21 of sample prepared with Eu_2O_3 as the raw material under a carbothermal atmosphere

(IQE = 7.51%, EQE = 3.87%), as shown in Fig. 4f and S7. The XPS and QE results further suggest that employing EuS as a raw material in a N₂ atmosphere leads to improved stabilization of the valence states of Eu²⁺ and Yb³⁺ ions, thereby facilitating an NIR-II emission enhancement of Yb³⁺ ions.

2.5 The temperature-dependent NIR luminescence properties of CSSO: 1%Eu²⁺, 5%Yb³⁺ sample.

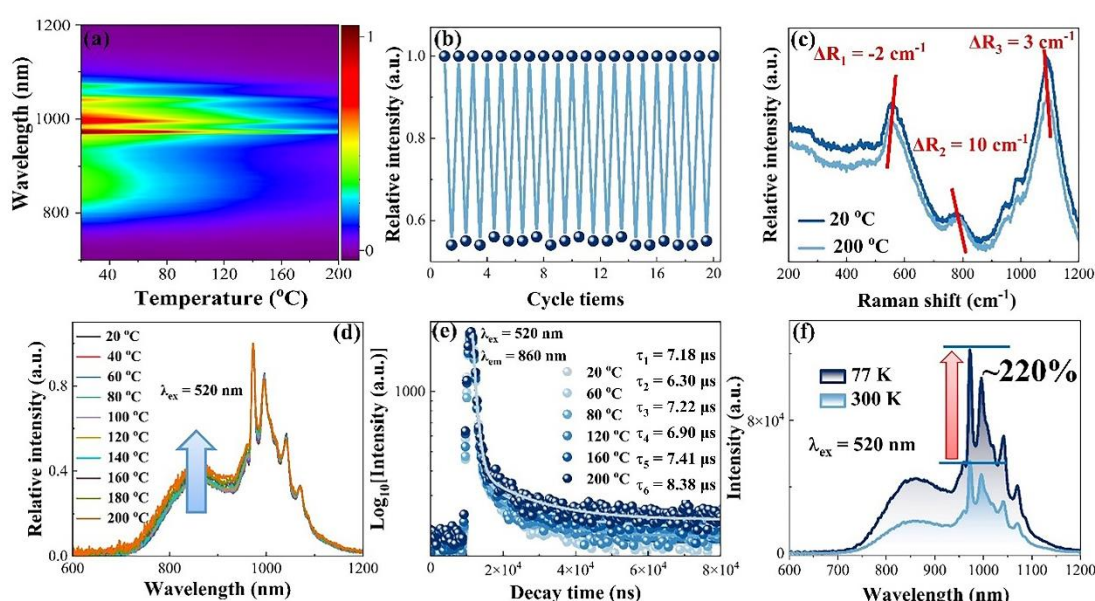


Figure 5(a) Temperature-dependent emission spectra mapping of CSSO: 1%Eu²⁺, 5%Yb³⁺ sample under 520 nm excitation; (b) Twenty cycles of intensity ratio variations measured at 120°C; (c) The variable temperature Raman spectra; (d) Normalized temperature-dependent emission spectra; (e) Decay curves in the temperature ranges of 30–200°C; (f) Emission spectra at 77 K and 300 K.

The temperature-dependent emission spectra of CSSO: 5%Yb³⁺ and CSSO: 1%Eu²⁺, 5%Yb³⁺ samples were thoroughly investigated, as depicted in Fig. 5a, S8-S10. Apparently, the NIR luminescence intensity of the CSSO: 1%Eu²⁺, 5%Yb³⁺ sample exhibits a downward trend as the temperature elevates from 30 to 200°C. At 120°C, the relative intensity is 55% of the initial value after twenty cycles test (Fig. 5b), which is lower than that of CSSO: 5%Yb³⁺ sample (95%@120°C). This is attributed to the

1 introduction of Eu^{2+} ions in the CSSO: 5% Yb^{3+} sample, which destroys the lattice order
2 in the crystal structure, significantly reducing the structural rigidity and resulting in
3 degenerate thermal stability.⁶¹ In addition, the temperature dependent Raman spectra
4 can directly reflect the variation in chemical bond vibrations of a sample.⁶² As shown
5 in Fig. 5c, at high temperature of 200°C, the SiO_4 tetrahedra exhibit significant bending
6 motions (ν_4), symmetric (ν_5) and asymmetric (ν_6) internal stretching vibrations. The
7 Raman shift ΔR is obvious, especially for the Raman peak at 790 cm^{-1} , which shift
8 reaches 10 cm^{-1} . This indicates the relatively weak rigidity of CSSO: 1% Eu^{2+} , 5% Yb^{3+}
9 sample, which further supports the above viewpoint.

10 The different thermal quenching behaviors of Eu^{2+} and Yb^{3+} ions emission centers
11 have also attracted our attention. As shown in Fig. 5d, by normalizing the emission peak
12 of Yb^{3+} (976 nm), it is observed that the emission intensity of Eu^{2+} (860 nm) gradually
13 increased, which is attributed to the phonon-assisted tunneling from the excited state of
14 Yb^{3+} to Eu^{2+} ions.⁶³ In order to analyze this phenomenon, we have tested the decay
15 curve within the temperature range of 30 to 200°C as illustrated in Fig. 5e. Generally,
16 with the increase of temperature and the energy transfer between Eu^{2+} and Yb^{3+} ions,
17 the decay time of Eu^{2+} should gradually decreases.^{55, 64} However, the calculated decay
18 time does not decrease with increase of temperature. Instead, it shows an irregular up
19 and down change around the average value 7.23 μs . This phenomenon indicates a
20 competitive relationship between the thermal quenching of Eu^{2+} ions and the energy
21 transfer of Eu^{2+} and Yb^{3+} ions in CSSO: 1% Eu^{2+} , 5% Yb^{3+} sample.²⁹ Furthermore, we

have also measured the emission spectra of CSSO: 1%Eu²⁺, 5%Yb³⁺ samples at 77 K, as shown in Fig. 5f. The results show that there is no obvious change in the peak shape of the emission spectrum at low temperature, but the emission intensity is 220% higher than that at 300 K.

2.6 Performance and application of the fabricated NIR-II pc-LED.

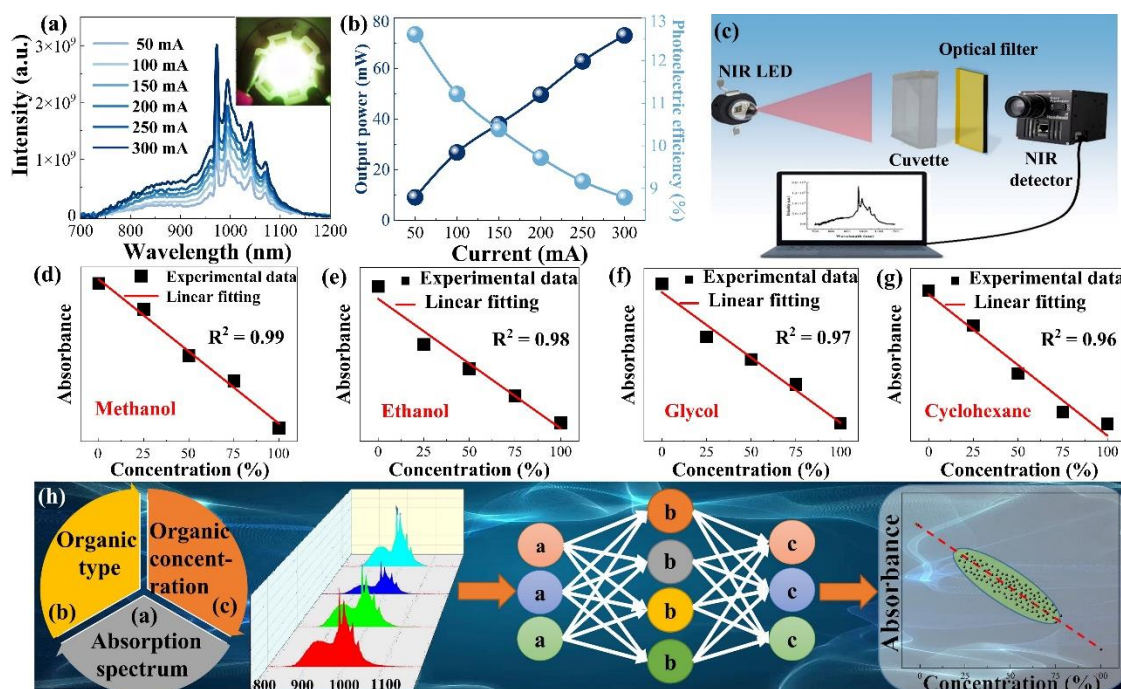


Figure 6 (a) and (b) PL spectra, output power and photoelectric efficiency of the fabricated NIR-II pc-LED under drive current of 50–300 mA; (c) Schematic diagram of the designed absorption spectroscopy testing system; The linear relationship between the absorbance and concentration of (d) methanol, (e) ethanol, (f) glycol and (g) cyclohexane; (h) The training and testing models of convolutional neural networks for the absorption spectra, types and concentrations of four organic solvents.

The NIR-II pc-LED is fabricated by combining the optimized CSSO: 1%Eu²⁺, 5%Yb³⁺ phosphor with a 520 nm LED chip. Fig. 6a and 6b display the PL spectra, output power, and photoelectric efficiency of the NIR-II pc-LED measured under drive currents ranging from 50 to 300 mA. The results show that the PL emission intensity increases significantly with the increase of current. The output power simultaneously

1 rises from 9.11 to 74.09 mW. Nevertheless, the photoelectric efficiency has decreased
2 from 12.61% to 8.79%. Additionally, we compared the electroluminescent properties
3 of our NIR-II pc-LED with similar green and blue light-excited NIR-II pc-LEDs, as
4 well as the commercial pc-NIR LEDs like Osram SHF 4735 and 4737, as detailed in
5 Table S4. The results reveal that the our NIR-II pc-LED demonstrates superior NIR
6 output power and photoelectric efficiency, which is not only significantly better than
7 other NIR-II pc-LEDs, but also comparable to the commercial Osram SHF 4737. The
8 operating temperature of the NIR-II pc-LED rises from 35.6 to 65.4°C as current rises
9 from 50 to 300 mA. When the NIR-II pc-LED is driven continuously at 100 mA for 30
10 to 120 min, its operating temperature increases from 37.7 to 60.1°C as shown in Fig.
11 S11. The minimal temperature variation of the NIR-II pc-LED during operation
12 highlights its potential as a high-power NIR light source suitable for scientific and
13 technical applications.²⁹

14 In order to highlight the potential application value of NIR-II pc-LED in the field
15 of NIR spectroscopy technology, we designed and constructed a miniaturized, real-time
16 absorption spectroscopy testing system using this NIR-II pc-LED as the light source as
17 shown in Fig. 6c. Since C-H, N-H, O-H and other functional groups with different
18 energy levels in organic molecules absorb NIR light at their specific vibrational
19 frequencies.^{11,65} Therefore, we tested four organic solvents using this homemade device
20 and determined their absorption spectra. As shown in Fig. S12, the absorption of
21 methanol and ethanol is mainly concentrated between 900 and 1100 nm,⁶⁶ the

absorption of glycol is mainly concentrated in the range of 800 to 1050 nm,⁶⁷ and cyclohexane only has an absorption peak at 930 nm.⁶⁸ Furthermore, the absorption spectra show a typical linear relationship with the change of concentration, conforming to the Lambert-Beer law, which proves its accuracy in the detection of the concentration of organic substances, and the goodness of fit and fitting formula as shown in Fig. 6d-6g and Eq. S1-S4. To further improve the accuracy of the organic solvent concentration tests, we have introduced a CNN model to learn from the measured absorption spectra, as shown in Fig. 6h. During the training phase, the CNN is trained to identify the absorption spectra of different concentrations of methanol, ethanol, glycol and cyclohexane (0, 25%, 50%, 75%, and 100%) to enhance its generalization ability. During the testing phase, we collected 100 different absorption spectra at various concentrations for each organic solvent and performed 100 predictions, achieving a maximum accuracy of up to 98%. The successful prediction of organic solvent concentrations further highlights the significant advantages of the NIR-II pc-LED prepared by CSSO: 1%Eu²⁺, 5%Yb³⁺ sample, enabling its suitability for various portable NIR detection instruments.

3. Conclusion

In this work, the energy transfer from Eu²⁺ to Yb³⁺ ions are achieved through rational design to enable the excitation of Yb³⁺ ions by visible light. Importantly, we proposed a strategy for synthesizing a series of Ca₃Sc₂Si₃O₁₂: xEu²⁺, yYb³⁺ ($x = 0$ and 1%, $0 \leq y \leq 7\%$) samples under N₂ atmosphere by replacing Eu₂O₃ with EuS. This

1 strategy not only effectively enhances the valence stability of Eu^{2+} and Yb^{3+} ions, but
2 also enhances the NIR-II emission quantum efficiency of Yb^{3+} ions by approximately
3 6 times. Finally, we combined the optimized sample with a 520 nm LED chip to prepare
4 NIR-II pc-LED. The photoelectric efficiency is 12.61%@50 mA and the output power
5 is 74.09 mW@300 mA, which is better than the current commercial NIR-II pc-LEDs.
6 Additionally, thanks to the efficient NIR-II emission of CSSO: 1% Eu^{2+} , 5% Yb^{3+} sample,
7 and combined with CNN technology to accurately distinguish different concentrations
8 of organic solvents, the accuracy rate reaches 98%. In summary, this work successfully
9 achieved visible light excitation of Yb^{3+} ions through the establishment of an “ Eu^{2+}
10 bridge”, which opened up a new way for the application of Yb^{3+} ions in the field of
11 portable NIR-II light source.

12 **Acknowledgements**

13 This work was supported by the National Key Research and Development
14 Program of China (Grant No. 2024YFA1409900), National Natural Science Foundation
15 of China (Grant Nos. U21A2074, U24A2018, U21A2068, 62375038, 12174046 and
16 12274057), Science and Technique Foundation of Dalian (Grant Nos. 2022JJ11CG003,
17 2023JJ12GX011 and 2022JJ12GX041), Science and Technique Foundation of Liaoning
18 Province (Grant Nos. 2023JH1/10400057, 2023JH1/10400080, 2023JH2/101800033,
19 2023JH2/101700058, 2023JH2/101700239 and 2024JH2/102400021) and
20 Fundamental Research Funds for the Central Universities (Grant No. 04442024068).

21

References

1. F. F. Wang, Y. T. Zhong, O. Bruns, Y. Y. Liang, H. J. Dai, *Nat. Photonics* **2024**, *18*, 535.
2. Y. Xie, W. S. Liu, W. Y. Deng, H. M. Wu, W. P. Wang, Y. C. Si, X. W. Zhan, G. Gao, X. K. Chen, H. B. Wu, J. B. Peng, Y. Cao, *Nat. Photonics* **2022**, *16*, 752.
3. S. K. Gupta, K. Sudarshan, R. M. Kadam, *Mater. Today. Commun.* **2021**, *27*, 102277.
4. S. Q. Liu, J. X. Du, Z. Song, C. G. Ma, Q. L. Liu, *Light: Sci. Appl.* **2023**, *12*, 181.
5. T. Z. Wang, Y. Z. Wang, W. B. Chen, Z. G. Xia, *Laser. Photonic. Rev.* **2024**, *18*, 2300784.
6. Z. W. Li, G. Zhu, S. S. Li, W. Xu, Q. F. Bian, Y. Cong, M. He, X. X. Luo, S. Y. Xin, B. Dong, *Laser. Photonic. Rev.* **2023**, *18*, 2300732.
7. D. P. Wang, L. Q. Yan, G. Zhu, S. Ma, N. Zhou, S. S. Li, Z. W. Li, Y. Cong, X. Bai, X. G. Han, B. Dong, *Laser. Photonic. Rev.* **2024**, 2401256.
8. G. C. Liu, Z. G. Xia, *J. Phys. Chem. Lett.* **2022**, *13*, 5001.
9. X. Ding, Q. Zhang, Z. H. Li, M. Yu, *J. Mater. Chem. C.* **2021**, *9*, 16022.
10. M. Zhao, S. Q. Liu, H. Cai, F. Y. Zhao, Z. Song, Q. L. Liu, *Sci. China. Mater.* **2022**, *65*, 748.
11. G. C. Liu, M. S. Molokeev, Z. G. Xia, *Chem. Mater.* **2022**, *34*, 1376.
12. W. Y. Zhou, J. B. Luo, J. Q. Fan, H. W. Pan, S. X. Zeng, L. Y. Zhou, Q. Pang, X. G. Zhang, *Ceram. Int.* **2021**, *47*, 25343.

13. J. Ren, F. M. Zhu, Y. Gao, J. B. Qiu, *Ceram. Int.* **2024**, *50*, 31474.
14. E. H. Song, H. Ming, Y. Y. Zhou, F. Q. He, J. C. Wu, Z. G. Xia, Q. Y. Zhang, *Laser. Photonic. Rev.* **2021**, *15*, 2000410.
15. Z. X. Wu, X. X. Han, Y. Y. Zhou, K. Xing, S. Cao, L. Chen, R. S. Zeng, J. L. Zhao, B. S. Zou, *Chem. Eng. J.* **2022**, *427*, 131740.
16. S. K. Gupta, R. M. Kadam, P. K. Pujari, *Coord. Chem. Rev.* **2020**, *420*, 213405.
17. Z. B. Tang, F. Du, H. Liu, Z. H. Leng, X. Q. Sun, H. D. Xie, M. D. Que, Y. H. Wang, *Adv. Opt. Mater.* **2022**, *10*, 2102204.
18. Z. B. Tang, Q. Zhang, Y. X. Cao, Y. X. Li, Y. H. Wang, *Chem. Eng. J.* **2020**, *388*, 124231.
19. G. C. Liu, W. B. Chen, Z. Xiong, Y. Z. Wang, S. Zhang, Z. G. Xia, *Nat. Photonics* **2024**, *18*, 562.
20. Q. H. Zhang, X. Wei, J. B. Zhou, B. Milićević, L. T. Lin, J. S. Huo, J. H. Li, H. Y. Ni, Z. X. Xia, *Adv. Opt. Mater.* **2023**, *11*, 2300310.
21. L. P. Jiang, D. Yang, L. L. Zhang, J. Wang, J. J. Zhang, W. W. Jiang, G. J. Li, H. B. Yu, W. Si, Z. X. Shi, Z. H. Zhang, Y. J. Su, *J. Alloys Compd.* **2025**, *1010*, 177826.
22. L. P. Jiang, L. L. Zhang, X. P. Zhao, X. Jiang, P. P. Gao, Y. J. Su, *Laser. Photonic. Rev.* **2024**, *18*, 2301226.
23. L. Q. Yan, G. Zhu, S. Ma, S. S. Li, Z. W. Li, X. X. Luo, B. Dong, *Laser. Photonic. Rev.* **2024**, *18*, 2301200.
24. G. Boulon, *J. Alloy. Compd.* **2008**, *451*, 1.

- 1 25. Y. J. Wang, X. J. Zhou, J. Shen, X. Q. Zhao, B. Wu, S. Jiang, L. Li, *J. Am. Ceram.*
2 *Soc.* **2016**, 99, 115.
- 3 26. M. Derksen, S. Bergkamp, O. Kohnstamm, E. V. D. Kolk, *Opt. Mater.* **2024**, 157,
4 116220.
- 5 27. J. Y. Shang, X. S. Xu, K. C. Liu, Y. N. Bao, B. Ding, *J. Alloy. Compd.* **2019**, 785,
6 610.
- 7 28. S. He, L. L. Zhang, H. Wu, H. J. Wu, G. H. Pan, Z. D. Hao, X. Zhang, L. G. Zhang,
8 H. Zhang, J. H. Zhang, *Adv. Opt. Mater.* **2020**, 8, 1901684.
- 9 29. Y. Zhang, S. H. Miao, Y. J. Liang, C. Liang, D. X. Chen, X. H. Shan, K. N. Sun, X.
10 J. Wang. *Light: Sci. Appl.* **2022**, 11, 136.
- 11 30. L. P. Jiang, X. Jiang, J. H. Xie, H. Y. Sun, L. L. Zhang, X. L. Liu, Z. H. Bai, G. C.
12 Lv, Y. J. Su, *J. Alloy. Compd.* **2022**, 920, 165912.
- 13 31. D. Zhang, B. F. Zheng, Z. B. Zheng, L. Li, Q. Yang, Y. H. Song, B. Zou, H. F. Zou,
14 *Chem. Eng. J.* **2022**, 431, 133805.
- 15 32. R. Mani, H. D. Jiang, S. K. Gupta, Z. Q. Li, X. L. Duan, *Inorg. Chem.* **2018**, 57,
16 935.
- 17 33. R. Mani, S. K. Gupta, P. S. Ghosh, H. D. Jiang, *Chem-Eur. J.* **2018**, 24, 16149.
- 18 34. R. J. Ji, T. Seto, Y. H. Wang, *J. Rare. Earths.* **2024**.
19 <https://doi.org/10.1016/j.jre.2024.09.012>.
- 20 35. X. K. Zou, H. R. Zhang, W. Li, M. T. Zheng, M. S. Molokeev, Z. G. Xia, Y. J.
21 Zheng, Q. M. Li, Y. L. Liu, X. J. Zhang, B. F. Lei, *Adv. Opt. Mater.* **2022**, 10, 2200882.

- 1 36. S. X. Wang, Z. Song, Q. L. Liu, *J. Mater. Chem. C* **2023**, *11*, 48.
- 2 37. J. W. Qiao, G. J. Zhou, Y. Y. Zhou, Q. Y. Zhang, Z. G. Xia, *Nat. Commun.* **2019**,
3 *10*, 5267.
- 4 38. Y. Wang, Z. J. Wang, G. H. Wei, Y. B. Yang, S. X. He, J. H. Li, Y. W. Shi, R. Li, J.
5 W. Zhang, P. L. Li, *Chem. Eng. J.* **2022**, *437*, 135346.
- 6 39. Y. N. Wang, Z. Xu, M. M. Shang, Y. X. Sun, X. L. Xing, P. P. Dang, J. Lin,
7 *Laser. Photonic. Rev.* **2024**, *18*, 2400295.
- 8 40. A. Balhara, S. K. Gupta, B. Modak, A. K. Yadav, B. S. Naidu, K. Sudarshan, *ACS*
9 *Appl. Mater. Interfaces.* **2025**, *17*, 1509.
- 10 41. L. Zhou, P. A. Tanner, W. J. Zhou, Y. Y. Ai, L. X. Ning, M. M. Wu, H. B. Liang,
11 *Angew. Chem. Int. Ed.* **2017**, *56*, 10357.
- 12 42. Z. X. Qiu, H. Z. Lian, M. M. Shang, S. X. Lian, J. Lin, *CrystEngComm.* **2016**, *18*,
13 4597.
- 14 43. R. D. Shannon, *Acta Crystallographica.* **1976**, *A32*, 751.
- 15 44. Z. W. Li, G. Zhu, F. Li, Q. Zhu, Y. Cong, X. Bai, J. G. Li, B. Dong, *J. Colloid.*
16 *Interf. Sci.* **2025**, *678*, 209.
- 17 45. J. J. Velázquez, R. F. González, J. M. Jerez, V. D. Rodríguez, A. Lukowiak, A.
18 Chiappini, A. Chiasera, M. Ferrari, P. Núñez, *Opt. Mater.* **2015**, *46*, 109.
- 19 46. F. Piccinelli, A. Speghini, G. Mariotto, L. Bovo, M. Bettinelli, *J. Rare. Earths.* **2009**,
20 *27*, 555.
- 21 47. C. Jiang, Q. Liu, K. Y. Li, Y. B. Feng, Y. K. Fu, Y. Li, Y. C. Zhang, X. Qian, B. Wei,

- 1 P. Du, *Chem. Eng. J.* **2024**, *496*, 154360.
- 2 48. S. Q. Fang, T. C. Lang, T. Han, J. Y. Wang, J. Y. Yang, S. X. Cao, L. L. Peng, B. T.
- 3 Liu, A. N. Yakovlev, V. I. Korepanov, *Chem. Eng. J.* **2020**, *389*, 124297.
- 4 49. M. J. Zhao, Y. T. Tao, P. T Wang, W. C. Li, D. P. Chen, W. Chen, *Ceram. Int.* **2024**,
- 5 *50*, 1857.
- 6 50. A. Balhara, S. K. Gupta, G. D. Patra, B. Modak, J. Prakash, K. Sudarshan, M.
- 7 Mohapatra, *Phys. Chem. Chem. Phys.* **2023**, *25*, 1889.
- 8 51. W. W. Ji, M. H. Lee, L. Y. Hao, X. Xu, S. Agathopoulos, D. W. Zheng, C. H. Fang,
- 9 *Inorg. Chem.* **2015**, *54*, 1556.
- 10 52. T. Xie, H. X. Guo, J. Y. Zhang, Y. N. He, H. Lin, G. L. Chen, Z. S. Zheng, *J. Lumin.*
- 11 **2016**, *170*, 150.
- 12 53. T. L. Wang, P. F. Zhang, J. Q. Xiao, Z. Y. Guo, X. W. Xie, J. H. Huang, J. J. Zheng,
- 13 X. H. Xu, L. Zhao, *Adv. Sci.* **2024**, 2410673.
- 14 54. L. P. Jiang, L. L. Zhang, X. Jiang, J. H. Xie, G. C. Lv, Y. J. Su, *Adv. Mater. Technol-*
- 15 *US.* **2024**, *9*, 2301495.
- 16 55. J. Y. Sun, Y. N. Sun, J. H. Zeng, H. Y. Du, *Opt. Mater.* **2013**, *35*, 1276.
- 17 56. D. Wang, B. Xue, J. Song, J. L. Qu, *J. Mater. Chem. C.* **2018**, *6*, 6597.
- 18 57. J. Z. Cui, Y. F. Wen, R. C. Chen, X. Cheng, M. D. Yu, J. D. Liu, Z. F. Hu, J. J. He,
- 19 Z. H. Xiao, X. Y. Sun, *Chem. Eng. J.* **2024**, *489*, 151416.
- 20 58. S. Schmidt, S. Hufner, F. Reinert, W. Assmus, *Phys. Rev. B: Condens. Matter Mater.*
- 21 *Phys.* **2005**, *71*, 195110.

- 1 59. Y. Ohno, *J. Electron. Spectrosc.* **2008**, *165*, 1.
- 2 60. L. A. Zavala, P. Fernández, E. Novitskaya, J. N. Díaz, M. Herrera, O. A. Graeve,
3 *Acta. Mater.* **2017**, *135*, 35.
- 4 61. D. W. Wen, H. M. Liu, Y. Guo, Q. G. Zeng, M. M. Wu, R. S. Liu, *Angew. Chem.*
5 *Int. Ed.* **2022**, *61*, e202204411.
- 6 62. Z. W. Li, G. Zhu, S. S. Li, S. Y. Xin, W. Xu, X. X. Luo, M. He, B. Dong, *Ceram.*
7 *Int.* **2023**, *49*, 21510.
- 8 63. H. P. Zhou, Q. P. Wang, Y. Jin, *J. Mater. Chem. C.* **2015**, *3*, 11151.
- 9 64. V. Jarý, L. Havlák, J. Bárta, E. Mihóková, M. Nikl, *Chem. Phys. Lett.* **2013**, *574*,
10 61.
- 11 65. L. L. Zhang, D. D. Wang, Z. D. Hao, X. Zhang, G. H. Pan, H. J. Wu, J. H. Zhang,
12 *Adv. Opt. Mater.* **2019**, *7*, 1900185.
- 13 66. Y. Yang, Z. Z. Lu, H. Fan, M. H. Chen, L. W. Shen, X. G. Zhang, Q. Pang, J. H.
14 Chen, P. C. Chen, L. Y. Zhou, *Inorg. Chem.* **2023**, *62*, 3601.
- 15 67. L. M. Fang, L. P. Lu, L. L. Zhang, H. Wu, H. J. Wu, G. H. Pan, Z. D. Hao, J. H.
16 Zhang, *Ceram. Int.* **2024**, *50*, 47733.
- 17 68. L. M. Fang, L. L. Zhang, H. Wu, H. J. Wu, G. H. Pan, Z. D. Hao, F. Liu, J. H.
18 Zhang, *Inorg. Chem.* **2022**, *61*, 8815.
- 19